Temporal shaping of narrow-band picosecond pulses via noncolinear sum-frequency mixing of dispersion-controlled pulses

Randy Lemons,[1,2,*] Nicole Neveu,[1,†] Joseph Duris,[1] Agostino Marinelli,[1] Charles Durfee,[2] and Sergio Carbajo[1,‡]

[1]*SLAC National Accelerator Laboratory and Stanford University,*
2575 Sand Hill Rd, Menlo Park, California 94025, USA
[2]*Colorado School of Mines, 1500 Illinois St, Golden, Colorado 80401, USA*

A long-sought-after goal for photocathode electron sources has been to improve performance by temporally shaping the incident excitation laser pulse. The narrow bandwidth, short wavelength, and picosecond pulse duration make it challenging to employ conventional spectral pulse shaping techniques. We present a novel and efficient intensity-envelope shaping technique achieved during nonlinear upconversion through opposite-chirp sum-frequency mixing. We also present a numerical case study of the linac coherent light source-II photoinjector where transverse electron emittance is improved by at least 25%.

I. INTRODUCTION

Generation of picosecond optical laser pulses with tailored temporal intensity envelopes is a technically challenging task. Their narrow spectral bandwidth restricts methods that attempt to modify temporal intensity through spectral phase and their temporal duration is too short to exploit direct electronic modulation methods. However, picosecond duration pulses and shaping their temporal intensity profile is critically important for photoinjector-based electron instruments. Photoinjectors lie at the heart of a myriad of forefront scientific research areas and technologies in quantum electrodynamics [1,2], high-energy physics [3,4], ultrafast science [5–8], and medical technologies [9–11] among many others. Even though the operational requirements for applications dependent on photoinjectors can be vastly different, increased electron control and performance remains a central challenge as these various technologies are brought to new scientific and engineering frontiers. From large scale facilities such as storage rings [12], electron-electron colliders [3], and x-ray free electron lasers (XFELs) [13], to laboratory-scale instrumentation such as ultrafast electron diffraction [14] or transmission electron microscopy [15], electron generation in a photoinjector exists as the crucial first step and a

*rlemons@slac.stanford.edu
†nneveu@slac.stanford.edu
‡scarbajo@slac.stanford.edu

significant predictor of instrument performance. One foundational strategy to tailor the electron bunch phase space for greater uniformity and higher brightness is to control the shape of the optical pulses used for photoemission.

In photoinjectors, electrons are generated via the photoelectric effect with laser pulses comprised of light, typically in the deep ultraviolet (UV), whose photon energy lies above the work function of the cathode material. After photoemission, electrons' phase-space distribution evolves rapidly from the interaction with the external accelerating fields and their own internal coulombic forces [16]. As part of this process, the spatiotemporal distribution of the laser pulses effect the electron distribution, and thereby can be used to influence how the bunches will evolve as they are accelerated in vacuum. A key measure of electron bunch quality is its transverse emittance, ϵ_x, defined as [17]

$$\epsilon_x = \sqrt{\langle x_i^2 \rangle \langle x_i'^2 \rangle - \langle x_i^2 x_i'^2 \rangle}, \qquad (1)$$

where x is transverse position and x' is the corresponding angle with respect to the ideal trajectory. Generally, emittance reduction is beneficial to the electron beam brightness and any associated secondary emission processes, and can be therefore be used as a metric to optimize in determining spatiotemporal laser distributions [18].

In XFELs, in addition to low emittance ($< 1.5 \ \mu$m), it is particularly crucial to have electron bunches with narrow energy spread ($\Delta E/E < 10^{-3}$) and good spatial uniformity, as growth in these parameters can significantly decrease x-ray production in the undulators [19]. Beyond conventional Gaussian temporal and spatial distribution of the photoinjector laser pulses, other commonly sought-after laser distributions shown to reduce normalized transverse

emittance include flattop spatiotemporal profiles resembling cylinders [20] or three-dimensional ellipsoids such that the beam size and intensity vary as a function of time [21].

Existing shaping techniques rely on modifying or combining femtosecond pulses and can be split into either spectral techniques such as spatial-light modulators [22,23] or acousto-optic modulators [24,25], or temporal techniques such as pulse stackers [20,26]. Spectral methods are hindered by tailored phase structure being distorted during pulse amplification and upconversion if shaping in the infrared, limited spectral bandwidth if shaping in the UV, and by material damage threshold limitations in the mW-level [27]. On the other hand, intensity fluctuations inherent to temporal techniques have been shown to induce unwanted microbunching [28,29] on the electron bunch, resulting in increased emittance relative to Gaussian distributions. In order to operate at the correct wavelength, these lasers also typically employ a series of nonlinear conversion stages to upconvert infrared light to UV light below 270 nm [30–32]. Efficient nonlinear conversion is detrimentally affected by nonflat phase structure and can distort tailored temporal profiles, complicating shaping efforts. As such, these methods are limited in their applicability to high average power, 24/7 facilities, such as linac coherent light source (LCLS) where reliability is paramount.

We present an upconversion method that incorporates temporal shaping into a nonlinear conversion stage exploiting post-amplification phase manipulation, thereby circumventing the pitfalls of existing upconversion and shaping techniques. We utilize noncolinear sum frequency generation (Fig. 1) combining two highly dispersed pulses that result in a pulse with tunable temporal profile in duration and shape [33,34]. Here, we build on the elegant approach by Raoult *et al.* [35] of efficient narrow band second harmonic generation in thick crystals by adding

higher-order dispersion to simultaneously shape the output pulse duration. The output pulse is nearly transform limited and can be directly utilized for application or passed through further nonlinear conversions processes without distortion. As such, this method, which we call dispersion controlled nonlinear shaping (DCNS), can be broadly used to tailor pulses for the reduction of normalized transverse emittance in photoinjector-based instrumentation.

II. DISPERSION-CONTROLLED PULSES

To describe DCNS, we start off by expressing the electric field of a laser in frequency space as $E(\omega) = A(\omega)e^{i\varphi(\omega)}$, where $A(\omega)$ is the spectral amplitude and $\varphi(\omega)$ is the spectral phase as a function of angular frequency ω. The amplitude function is typically Gaussian in shape and the spectral phase is customarily described by a Taylor expansion around the central frequency of the field, ω_0.

$$\varphi(\omega) = \varphi_0 + \varphi_1(\omega - \omega_0) + \frac{\varphi_2}{2!}(\omega - \omega_0)^2$$
$$+ \frac{\varphi_3}{3!}(\omega - \omega_0)^3 + \frac{\varphi_4}{4!}(\omega - \omega_0)^4 + \cdots, \quad (2)$$

Here φ_j is the jth derivative of $\varphi(\omega)$, evaluated at ω_0.

The first two terms of Eq. (2) correspond to the absolute phase at the central frequency and the group delay, respectively. Since these two terms do not affect the shape of the pulses, our investigation will focus on the next terms, higher order in ω, to control the shape of the pulse envelope. The second-order dispersion (SOD) term, φ_2, is a quadratic phase that gives a linear ordering to the arrival time of the frequency components, stretching the duration of the pulse. Third-order dispersion (TOD) results from cubic phase, φ_3. Here, the opposite ends of the spectrum will overlap in time either before or after the main peak, leading to characteristic beating or temporal fringes. Higher orders effect the pulse similarly, but to a lesser degree, with even orders primarily effecting pulse duration and odd orders leading to modulation of the pulse in the time domain. In our description, we will focus on using a combination of SOD and TOD as the two most influential parameters to control the shape of the output pulse in the nonlinear sum frequency mixing process.

III. METHODS AND RESULTS

We begin by modeling these pulses as a combination of two equal-energy transform-limited Gaussian pulses overlapped in time. From here, the phase of each pulse can be adjusted separately by multiplying with Eq. (2) in frequency space, where φ_2 and φ_3 are free parameters and higher order terms are ignored. These tailored pulses then become our two initial fields, A_1 and A_2, used in solving the coupled equations [Eq. (3)] for sum frequency generation [36],
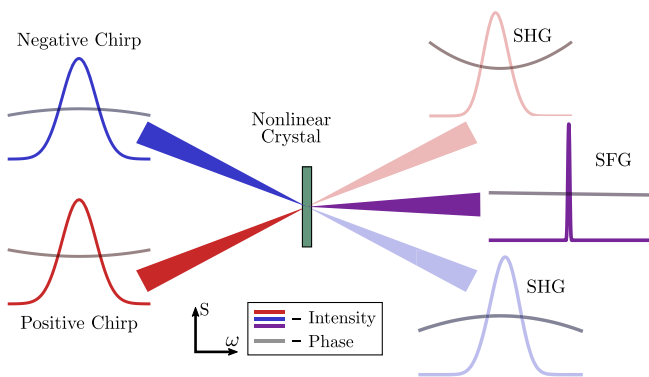

FIG. 1. DCNS method in the spectral domain demonstrating two pulses of equal on opposite chirp mixing in a nonlinear medium to generate chirped second harmonic (SHG) copies of each pulse along with the narrow band, flat phase, sum frequency (SFG) pulse.

$$\frac{dA_1}{dz} = \frac{2id_{\text{eff}}\omega_1^2}{k_1 c^2} A_2^* A_3 e^{-i\Delta kz}, \tag{3a}$$

$$\frac{dA_2}{dz} = \frac{2id_{\text{eff}}\omega_2^2}{k_2 c^2} A_1^* A_3 e^{-i\Delta kz}, \quad \text{and} \tag{3b}$$

$$\frac{dA_3}{dz} = \frac{2id_{\text{eff}}\omega_3^2}{k_3 c^2} A_1 A_2 e^{i\Delta kz}. \tag{3c}$$

Propagation and frequency mixing is handled using a symmetrized split-step Fourier method along with a fourth order Runga-Kutta algorithm to solve the coupled non-linear equations. Nonlinear conversion and nonlinear index effects are handled in the time and position domains while propagation and dispersion through the crystal are handled in the temporal and spatial frequency domain. To ensure accurate results, the resolution of the time, frequency, and spatial grids was increased until further refinement resulted in negligible change to the results.

As stated above, SOD primarily controls duration and TOD controls the sharpness of the leading or trailing edge and ringing in the field on the opposing edge. It is the interplay between SOD and TOD (Fig. 2) that then determines the pulse duration and the shape.

By defining the ratio between TOD and SOD,

$$\alpha = \frac{\varphi_3/ps^3}{\varphi_2/ps^2}, $$

we gain a single parameter to describe the general shape of a shaped pulse that is approximately invariant to pulse duration [37].
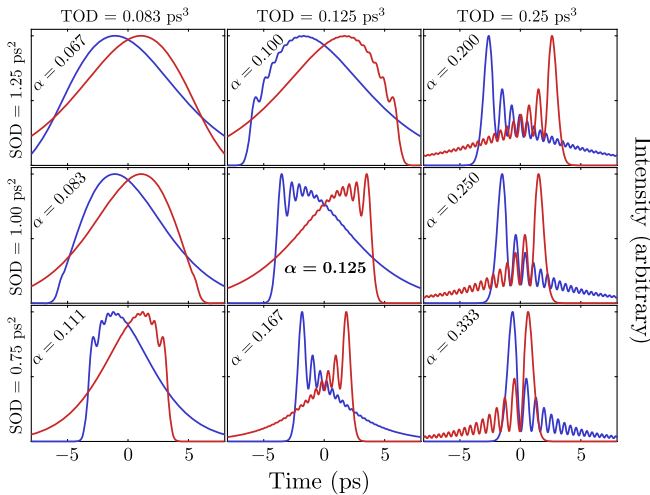

FIG. 2. Pulse envelopes resulting from different combinations of SOD and TOD. Each column has a the same magnitude of the TOD value at the top and each row has the same magnitude of SOD. The blue plot results from combinations with negative SOD and positive TOD while the red plot is positive SOD and negative TOD.

Applying these concepts in combination with narrow bandwidth generation suggested by Raoult *et al.* [35], we can search for pulses that fulfill our need for sharp rise time, long pulse duration, and narrow bandwidth.

To best illustrate our conversion scheme and to explore how it might be implemented in a real-world case, we use the photoinjector system at LCLS-II. This system consists of an Ytterbium-based commercial laser that outputs 50 μJ, 330 fs pulses with an approximately 4 nm full width at half maximum (FWHM) spectral bandwidth. We propose using type I noncollinear SFG in the conversion from 1030 to 515 nm. Using Fig. 2, as a reference to which portion of the pulses will mix, and considering that the LCLS-II design assumed a few 10s of picosecond flattop photoinjector laser pulse [38], we focus on situations where the magnitude of α is close to 0.125 ps (center column). This results in the signal and idler pulses having equal and opposite amounts of SOD and α = −0.128 ps, for temporal symmetry. The initial value of SOD (≈3.5 ps²) was chosen so that the FWHM of the 515 nm pulse would be 25 ps in time.

This large amount of SOD necessitates a large amount of TOD to maintain α. This can be achieved by passing the transform-limited pulses through a matched compressor-stretcher set with gratings detuned from Littrow angle. To maintain grating efficiency, one can generate a larger amount of SOD and an appropriate amount of TOD in the set and reduce SOD to desired levels afterward with highly dispersive optics, such as chirped volume Bragg gratings [39].

Once the half-pulse fields are constructed from the given phase parameters, they are propagated with the split-step method through β barium borate with the crystal angle tuned for type I sum mixing and a 2 mm crystal length. The crossing angle was set to 1.5 deg. This angle must be sufficiently large to allow the sum-frequency signal to be separated from the two input beams and suppress intrabeam second harmonic generation, but not so large as to reduce the spatial overlap of the beams in the crystal [35]. Additionally, the simulated focusing through the crystal was adjusted to eliminate back-conversion from 515 to 1030 nm as this process can distort the temporal and spectral profiles.

The resultant pulse [Fig. 3(a)] displays the attractive qualities of a sharp rise time and a flatter profile than the traditionally used Gaussian pulses with upward of 65% conversion efficiency in simulation. Experimental efficiency is likely to be less than the 40% stated by Raoult *et al.* [35] due to added TOD. It is also characterized by large and rapid amplitude fluctuations on the picosecond scale that can be detrimental to e-beam emittance. These fluctuations—the larger oscillations at the edges—are the result of coherent interaction between the main spectral peak and interference from the higher wavelengths in the asymmetric tail seen in Fig. 3(b). However, by applying a spectral amplitude filter after conversion that is significantly wider than the FWHM of the pulse's spectral
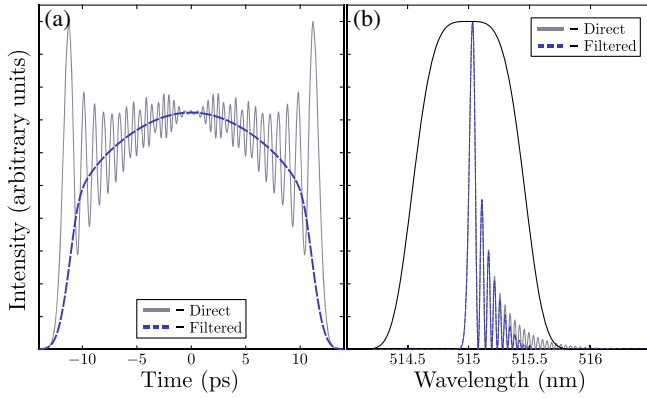
FIG. 3. Genetic algorithm optimized 515 nm laser profile for a bunch length of 1.22 mm resulting in an emittance value of 0.30 μm. Notably, the genetic algorithm settled on a profile which has slower rise and fall times than an ideal flat top as emittance is optimized rather than profile shape. The two plots shown are (a) the laser profile in time before (grey) and after (blue, dashed) a 0.5 nm spectral filter and (b) the spectrum of the pulse before (grey) and after filtering (blue, dashed) with the super-gaussian spectral filter in black.

bandwidth [Fig. 3(b)], the high-frequency components can be attenuated without a major efficiency penalty. In this case, employing a second order super-Gaussian spectral filter with $1/e$ width of 0.5 nm, such as a Bragg grating interference filter, the total power in the field is reduced by less than 10% and results in a smoother temporal profile [Fig. 3(a)]. As with the mixing, the numerical grids were chosen to reduce possible numerical errors from these filters. Alternatively, the thickness of the nonlinear crystal for the doubling step from 515 to 257 nm can be chosen to filter the bandwidth through phase mismatch [40].

To compare the performance of the DCNS pulses vs the baseline Gaussian temporal distribution, we simulated the LCLS-II photoinjector performance. To reduce simulation time, the DCNS temporal intensity profiles at 515 nm are squared to directly generate the UV profiles with a root mean squared error of less than 1% [37]. These pulses are supplied as the initial condition to the simulation and used to model the initial electron beam parameters. Electron bunch generation includes variations derived from oscillations in the laser pulse profile. The simulation code used for e-beam dynamics is OPAL [41], and for particle distribution generation, distgen [42]. The FWHM in time and spot size of the laser pulse directly impact the resulting three-dimensional shape of the emitted electron beam. As the beam is emitted, the forces due to external magnetic and electric fields along with internal space charge fields are computed at each time step. In this case, the FWHM is controlled by the magnitude of SOD and shape by α. While supplying the DCNS pulses is straightforward, determining the optimal FWHM and spot size of the pulse is not. The strength of the space charge forces are directly impacted by both the FWHM and spot size, which then impacts how

strong the external forces need to be to limit emittance growth. To determine optimal laser and machine settings, the parallel simulation code is run in combination with an optimization algorithm (NSGA-II [43]) using libEnsemble [44], a Python library that coordinates ensemble calculations. Standard optimization of the LCLS-II photoinjector includes variables such as laser spot size, laser FWHM, rf cavity phases, rf cavity gradients, and magnet strengths. To maintain broad applicability of these results, we limit the simulation to only the photoinjector and the first 15 m of acceleration ($\approx$100 MeV), after which are LCLS-II specific configurations. In this region, the laser parameters have the greatest impact on electron bunch evolution as internal space-charge forces are not yet damped by highly relativistic speeds.

The metrics commonly used for determining beam quality for XFELs are emittance (1) and bunch length (σ_z). If the emittance is extremely small, the beam size, momentum, or both must be small as well. Note, we do not optimize the orthogonal transverse dimension, y, because the simulation is transversely symmetric. As stated earlier, smaller emittances lead to brighter bunches and therefore better x-ray production. The same logic applies to second metric of interest, the bunch length, which is the rms size of the bunch in the longitudinal dimension. Shorter bunches require less compression after the injector, which mitigates nonlinearities in the bunch compression process and results in better FEL performance.

With these variables and metrics defined, several optimization rounds were performed to compare the performance of DCNS and Gaussian laser pulses in the LCLS-II photoinjector. Final results are shown in Figs. 4 and 5, with the later showing density of simulation points near the Pareto fronts. Figure 4 demonstrates that lower emittance
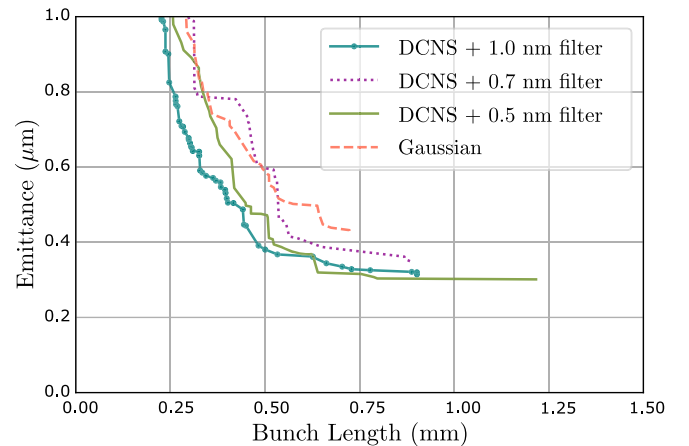

FIG. 4. Pareto front comparison of DCNS and Gaussian performance for the LCLS-II injector. DCNS pulses in combination with a 1.0 nm spectral filter, achieves the lowest emittance values at most bunch lengths. The lowest achieved emittance value is 0.30 μm at a bunch length of 1.22 mm, using a 0.5 nm filter.
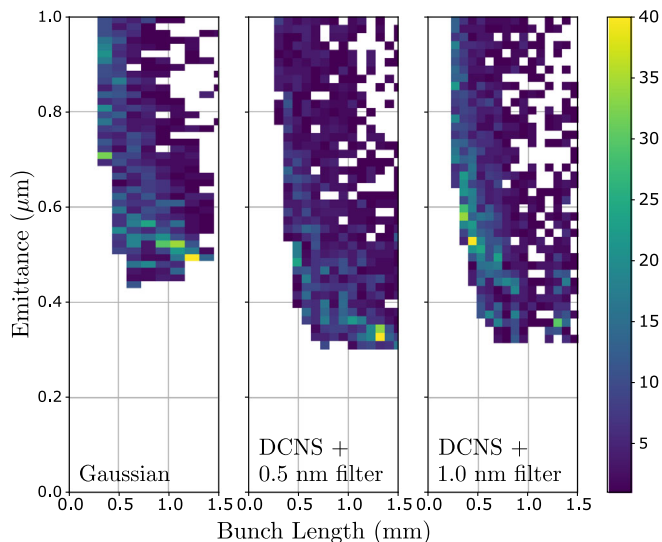
FIG. 5. Histogram showing simulation density of all GA solutions, not only Pareto optimal, for Gaussian and DCNS cases. Lighter colored areas indicate a higher number of simulations with valid solutions and thus regions where different methods might be more effective.

values are achieved using DCNS. Further, Fig. 5 indicates the density of low-emittance values are shifted for different filters. With a spectral filter of bandwidth 0.5 nm, longer bunch lengths are performing better, whereas with the 1.0 nm filter, there is a higher density of points at shorter bunch lengths. This suggests DNCS could benefit a variety of experimental XFEL configurations with the filter bandwidth and α used as an adjustment knob.

As shown in Fig. 4, the best value found is $\epsilon_x = 0.30$ μm with the DCNS pulse shown in Fig. 3. The bunch length in this case, 1.22 mm, is slightly longer than the typical operating length of 1 mm at LCLS. For a practical comparison, we choose the minimum emittance values at $\sigma_z = 1$ mm. A 25% improvement in the emittance value is obtained from DCNS ($\epsilon_x = 0.37$ μm) vs Gaussian ($\epsilon_x = 0.50$ μm) pulses. Note, this Gaussian point is not visible in Fig. 4, because it is not Pareto optimal. For shorter bunch lengths, i.e., 0.5 mm, the difference is slightly larger reaching about 30% ($\epsilon_x = 0.4$ vs 0.58 μm). Applying this reduction to both x and y planes, since the simulation is symmetric, the total transverse brightness can be more than doubled. In the case of XFELs, this emittance improvement translates to a twofold increase in undulator peak brightness, 25% shorter x-ray wavelengths, and an upper bound reduction in undulator lengths by 25% for similar peak currents, which can substantially reduce cost, complexity, and size.

IV. CONCLUSION

The regime of picosecond intensity envelope shaping is a challenging task that traditionally lies outside the capabilities of many methods commonly implemented for optical pulses with more spectral bandwidth or longer duration. Nonetheless, photoinjector-based electron sources, which would benefit from shaping in this regime, driving understanding of subatomic interactions, molecular structure, biological processes, and fundamental particle science utilize known suboptimal techniques. By tailoring the photoinjector drive lasers, electron emittance, and by extension the electron beam brightness, can be improved enabling further exploration of these research areas and the possibility for broad impact across multiple disciplines. Existing shaping techniques for the up-converted lasers used in the photoinjectors suffer from challenges in maintaining favorable pulse shapes, providing enough photon throughput for excitation, or even increasing electron emittance. Our proposed optical shaping and conversion technique, DCNS, circumvents these issues by directly upconverting optical pulses where the production of favorable temporal distributions is embedded in sum frequency conversion using highly dispersed pulses. In the case of linear accelerators and XFELs such the LCLS-II, this simple solution is expected to improve electron emittance across all investigated bunch lengths over conventional Gaussian pulses with an upward of 30% emittance reduction at short bunch lengths (0.25 mm) and 25% at bunch lengths greater than or equal to 1 mm. With an effective conversion efficiency of upward of 40%, we have laid a realistic avenue to substantially extend the brightness of photoinjector systems worldwide without major configuration changes and thus enhance current scientific capabilities on existing accelerators and reduce the cost of future accelerator facilities.

[1] V. Yakimenko, S. Meuren, F. Del Gaudio, C. Baumann, A. Fedotov, F. Fiuza, T. Grismayer, M. Hogan, A. Pukhov, L. Silva, and G. White, Prospect of Studying Nonperturbative QED with Beam-Beam Collisions, Phys. Rev. Lett. **122,** 190404 (2019).

[2] K. Wang, R. Dahan, M. Shentcis, Y. Kauffmann, A. B. Hayun, O. Reinhardt, S. Tsesses, and I. Kaminer, Coherent interaction between free electrons and a photonic cavity, Nature (London) **582,** 50 (2020).

[3] J. Ellis and I. Wilson, New physics with the compact linear collider, Nature (London) **409,** 431 (2001).

[4] W. P. Leemans, B. Nagler, A. J. Gonsalves, C. Tóth, K. Nakamura, C. G. Geddes, E. Esarey, C. Schroeder, and

S. Hooker, GeV electron beams from a centimetre-scale accelerator, Nat. Phys. **2**, 696 (2006).

[5] P. Emma *et al.*, First lasing and operation of an ångstrom-wavelength free-electron laser, Nat. Photonics **4**, 641 (2010).

[6] J. Kern *et al.*, Structures of the intermediates of Kok's photosynthetic water oxidation clock, Nature (London) **563**, 421 (2018).

[7] B. Stankus *et al.*, Ultrafast x-ray scattering reveals vibrational coherence following rydberg excitation, Nat. Chem. **11**, 716 (2019).

[8] M. Ibrahim *et al.*, Untangling the sequence of events during the s2 → s3 transition in photosystem II and implications for the water oxidation mechanism, Proc. Natl. Acad. Sci. U.S.A. **117**, 12624 (2020).

[9] R. Neutze, R. Wouts, D. Van der Spoel, E. Weckert, and J. Hajdu, Potential for biomolecular imaging with femtosecond x-ray pulses, Nature (London) **406**, 752 (2000).

[10] N. Coquelle *et al.*, Chromophore twisting in the excited state of a photoswitchable fluorescent protein captured by time-resolved serial femtosecond crystallography, Nat. Chem. **10**, 31 (2018).

[11] T. J. Wolf *et al.*, The photochemical ring-opening of 1, 3-cyclohexadiene imaged by ultrafast electron diffraction, Nat. Chem. **11**, 504 (2019).

[12] D. H. Bilderback, P. Elleaume, and E. Weckert, Review of third and next generation synchrotron light sources, J. Phys. B **38**, S773 (2005).

[13] B. W. McNeil and N. R. Thompson, X-ray free-electron lasers, Nat. Photonics **4**, 814 (2010).

[14] J. Hastings, F. Rudakov, D. Dowell, J. Schmerge, J. Cardoza, J. Castro, S. Gierman, H. Loos, and P. Weber, Ultrafast time-resolved electron diffraction with megavolt electron beams, Appl. Phys. Lett. **89**, 184109 (2006).

[15] R. Li and P. Musumeci, Single-shot MeV transmission electron microscopy with picosecond temporal resolution, Phys. Rev. Applied **2**, 024003 (2014).

[16] D. T. Palmer *et al.*, The next generation photoinjector, Ph.D. thesis, Citeseer, 1998.

[17] H. Wiedemann, Particle beams and phase space, in *Particle Accelerator Physics* (Springer International Publishing, Cham, 2015), pp. 213–251.

[18] F. Stephan and M. Krasilnikov, High brightness photo injectors for brilliant light sources, in *Synchrotron Light Sources and Free-Electron Lasers: Accelerator Physics, Instrumentation and Science Applications* (Springer, New York, 2020), pp. 603–646, https://doi.org/10.1007/978-3-319-14394-1.

[19] Z. Huang and K.-J. Kim, Review of x-ray free-electron laser theory, Phys. Rev. ST Accel. Beams **10**, 034801 (2007).

[20] M. Krasilnikov *et al.*, Experimentally minimized beam emittance from an l-band photoinjector, Phys. Rev. ST Accel. Beams **15**, 100701 (2012).

[21] O. Luiten, S. Van der Geer, M. De Loos, F. Kiewiet, and M. Van Der Wiel, How to Realize Uniform Three-Dimensional Ellipsoidal Electron Bunches, Phys. Rev. Lett. **93**, 094802 (2004).

[22] S. Y. Mironov, A. Potemkin, E. Gacheva, A. Andrianov, V. Zelenogorskii, M. Krasilnikov, F. Stephan, and E. Khazanov, Shaping of cylindrical and 3d ellipsoidal beams for electron photoinjector laser drivers, Appl. Opt. **55**, 1630 (2016).

[23] G. Penco *et al.*, Optimization of a high brightness photoinjector for a seeded fel facility, J. Instrum. **8**, P05015.

[24] Y. Li, S. Chemerisov, and J. Lewellen, Laser pulse shaping for generating uniform three-dimensional ellipsoidal electron beams, Phys. Rev. ST Accel. Beams **12**, 020702 (2009).

[25] M. Petrarca, P. Musumeci, M. Mattioli, C. Vicario, G. Gatti, A. Ghigo, S. Cialdi, and I. Boscolo, Production of temporally flat top UV laser pulses for sparc photoinjector, in *International Conference on Charged and Neutral Particles Channeling Phenomena II* (International Society for Optics and Photonics, Bellingham, 2007), Vol. 6634, p. 66341I.

[26] M. Krasilnikov, Y. Chen, and F. Stephan, Studies of space charge dominated electron photoemission at pitz, in *Journal of Physics: Conference Series*, Vol. 1238 (IOP Publishing, Bristol, 2019), p. 012064.

[27] S. Carbajo and K. Bauchert, Power handling for LCoS spatial light modulators, in *Laser Resonators, Microresonators, and Beam Control XX*, Vol. 10518 (International Society for Optics and Photonics, Bellingham, 2018), p. 105181R.

[28] S. Bettoni, M. C. Divall, R. Ganter, M. Pedrozzi, E. Prat, S. Reiche, T. Schietinger, A. Trisorio, C. Vicario, and V. Goryashko, Impact of laser stacking and photocathode materials on microbunching instability in photoinjectors, Phys. Rev. Accel. Beams **23**, 024401 (2020).

[29] C. Mitchell, P. Emma, J. Qiang, and M. Venturini, Sensitivity of the microbunching instability to irregularities in cathode current in the LCLS-II beam delivery system, in *Proceedings of NAPAC2016* (JACoW, Geneva, 2016).

[30] I. Will, H. I. Templin, S. Schreiber, and W. Sandner, Photoinjector drive laser of the flash FEL, Opt. Express **19**, 23770 (2011).

[31] S. Gilevich *et al.*, The LCLS-II photo-injector drive laser system, in *2020 Conference on Lasers and Electro-Optics (CLEO)* (IEEE, Piscataway, 2020), pp. 1–2.

[32] R. Alley *et al.*, The design for the LCLS rf photoinjector, Nucl. Instrum. Methods Phys. Res., Sect. A **429**, 324 (1999).

[33] C. Vicario, A. Trisorio, G. Arisholm, and C. P. Hauri, Deep-ultraviolet picosecond flat-top pulses by chirp-matched sum frequency generation, Opt. Lett. **37**, 1619 (2012).

[34] I. Kuzmin, S. Y. Mironov, M. Martyanov, A. Potemkin, and E. Khazanov, Highly efficient fourth harmonic generation of broadband laser pulses retaining 3d pulse shape, Appl. Opt. **60**, 3128 (2021).

[35] F. Raoult, A. Boscheron, D. Husson, C. Sauteret, A. Modena, V. Malka, F. Dorchies, and A. Migus, Efficient generation of narrow-bandwidth picosecond pulses by frequency doubling of femtosecond chirped pulses, Opt. Lett. **23**, 1117 (1998).

[36] R. W. Boyd, *Nonlinear Optics* (Academic Press, New York, 2019).

[37] See Supplemental Material at http://link.aps.org/supplemental/10.1103/PhysRevAccelBeams.25.013401 for reference figure; for quantitative analysis.

[38] J. Stohr, Linac Coherent Light Source II (LCLS-II) conceptual design report, 2011, https://www.osti.gov/biblio/1029479.

[39] A. Galvanauskas, A. Heaney, T. Erdogan, and D. Harter, Use of volume chirped Bragg gratings for compact high-energy chirped pulse amplification circuits, in *Technical Digest. Summaries of Papers Presented at the Conference on Lasers and Electro-Optics. Conference Edition. 1998 Technical Digest Series, Vol. 6 (IEEE Cat. No. 98CH36178)* (IEEE, Piscataway, 1998), p. 362.

[40] C. Radzewicz, P. Wasylczyk, and J. Krasinski, A poor man's frog, Opt. Commun. 186, 329 (2000).

[41] A. Adelmann, P. Calvo, M. Frey, A. Gsell, U. Locans, C. Metzger-Kraus, N. Neveu, C. Rogers, S. Russell, S. Sheehy, J. Snuverink, and D. Winklehner, Opal a versatile tool for charged particle accelerator simulations, arXiv:1905.06654.

[42] C. Gulliford, DistGen: Particle distribution generator (2019).

[43] K. Deb, A. Pratap, S. Agarwal, and T. Meyarivan, A fast and elitist multiobjective genetic algorithm: NSGA-II, IEEE Trans. Evol. Comput. 6, 182 (2002).

[44] S. Hudson, J. Larson, S. M. Wild, D. Bindel, and J.-L. Navarro, libEnsemble Users Manual, Technical Report Revision 0.7.1 (Argonne National Laboratory, Lemont, 2021).